MASSIVE YOUNG STELLAR OBJECT W42-MME: THE DISCOVERY OF AN INFRARED JET USING VLT/NACO NEAR-INFRARED IMAGES

L. K. DEWANGAN[1], Y. D. MAYYA[1], A. LUNA[1], AND D. K. OJHA[2]

[1] Instituto Nacional de Astrofsica, Óptica y Electrónica, Luis Enrique Erro # 1, Tonantzintla, Puebla, México C.P. 72840, México; lokeshd@inaoep.mx
[2] Department of Astronomy and Astrophysics, Tata Institute of Fundamental Research, Homi Bhabha Road, Mumbai 400 005, India

ABSTRACT

We report on the discovery of an infrared jet from a deeply embedded infrared counterpart of the 6.7 GHz methanol maser emission (MME) in W42 (i.e., W42-MME). We show that W42-MME drives a parsec-scale H_2 outflow, with the detection of a bow shock feature at ~0.52 pc to the north. The inner ~0.4 pc part of the H_2 outflow has a position angle of ~18° and the position angle of ~40° is found farther away on either side of the outflow from W42-MME. W42-MME is detected at wavelengths longer than 2.2 μm and is a massive young stellar object with an estimated stellar mass of $19 \pm 4\,M_\odot$. We map the inner circumstellar environment of W42-MME using Very Large Telescope (VLT)/NACO adaptive optics K_s and L' observations at resolutions of ~0″2 and ~0″1, respectively. We discover a collimated jet in the inner 4500 AU using the L' band, which contains prominent Brα line emission. The jet is located inside an envelope/cavity (extent ~10,640 AU) that is tapered at both ends and is oriented along the north–south direction. Such observed morphology of the outflow cavity around the massive star is scarcely known and is very crucial for understanding the jet-outflow formation process in massive star formation. Along the flow axis, which is parallel to the previously known magnetic field, two blobs are found in both the NACO images at distances of ~11800 AU, located symmetrically from W42-MME. The observed W42-MME jet-outflow configuration can be used to constrain the jet launching and jet collimation models in massive star formation.

Key words: HII regions – ISM: individual objects (W42-MME) – ISM: jets and outflows – ISM: magnetic fields – stars: formation

1. INTRODUCTION

The driving mechanism of jets and their role in massive star formation (MSF) is still subject to considerable debate. Outflows are a ubiquitous feature of MSF (Lada 1985; Beuther et al. 2002; Zhang et al. 2005). There has been an increasing number of detections of molecular outflows from massive protostars (e.g., Beuther et al. 2002, 2009; Wu et al. 2004; Zhang et al. 2005; Arce et al. 2007), which suggests that they are formed through the accretion process. However, the number of known massive young stellar objects (MYSOs) associated with collimated jets is very limited (see Guzmán et al. 2010 for more details). Additionally, information concerning the magnetic field toward the MYSO jet/outflow system is scarcely available (e.g., Jones et al. 2004; Carrasco-González et al. 2010). The investigation of MSF is often handicapped by the fact that massive stars are statistically rare, situated at large distances ($\geqslant 1$ kpc), present in clustered environments, and suffer from high extinction. All of these factors inhibit their observational study in the early phases. Key to overcoming these difficulties is the high angular resolution observations toward candidate massive protostars at infrared and longer wavelengths, which will allow mapping of the inner circumstellar environment. It has been well established that the 6.7 GHz methanol maser emission (MME) is associated with early phases of MSF (e.g., Walsh et al. 1998; Urquhart et al. 2013) and hence traces the locations of MYSOs. Therefore, such sites are very promising to carry out a detailed study to understand the involved physical processes of MSF.

W42 is a galactic giant HII region (G25.38–0.18) harboring a spectroscopically classified O5–O6 star in the heart of a near-infrared (NIR) cluster (Blum et al. 2000). Distances reported for W42 range from 2.2 kpc, as obtained by Blum et al. (2000)

assuming the O-star is in the zero-age main sequence (ZAMS), to 3.8 kpc, which was obtained kinematically using the radio recombination line H86α from the HII region (59.1 km s^{-1}; Lester et al. 1985) and the CO line from the associated cloud (58–69 km s^{-1}; Anderson et al. 2009). Using the K-band polarimetric image toward the NIR cluster in W42, Jones et al. (2004) discovered a bipolar reflection nebula that is illuminated by an undetected source at ~10″ south–west of the O-star. Based on the alignment of the long axis of the nebula with the magnetic field at the position angle of ~15°, they argued that the reflection nebula is tracing a bipolar outflow driven by an embedded young stellar object (YSO) that is hidden by a cloud with an extinction of $A_V > 55$ mag. However, they did not find any K-band counterpart of the driving source. We found that a 6.7 GHz MME detected by Szymczak et al. (2012) lies close to the predicted position of the driving source. We trace the reflection nebula as a parsec-scale bipolar outflow in the H_2 (1–0) S(1) 2.12 μm continuum-subtracted image (see Figure 1). The line-of-sight velocity of the MME is ~58.1 km s^{-1}, very similar to the velocity of the HII region. Considering the fact that the 6.7 GHz maser is physically associated with W42, a distance of 3.8 kpc is also adopted for MME in this paper. The presence of a parsec-scale outflow around 6.7 GHz MME makes this system ideal for exploring the early phases of MSF, including looking for a jet using high angular resolution NIR imaging.

In this paper, using multi-wavelength archival data, we investigate an infrared counterpart (IRc) of 6.7 GHz MME (hereafter W42-MME) and present observational evidence for W42-MME as an MYSO with a jet at the base of a parsec-scale bipolar H_2 outflow. The presence of a jet is investigated using
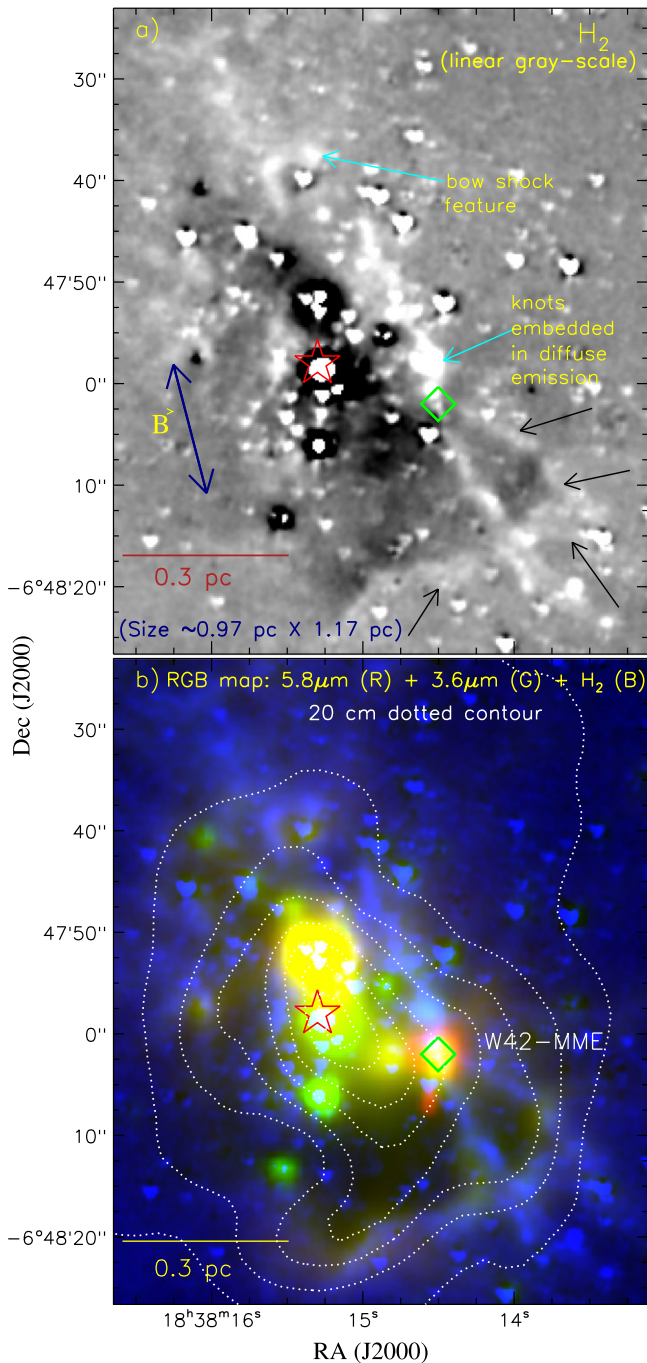
Figure 1. (a) Continuum-subtracted H_2 (1–0) S(1) 2.12 μm image illustrating the outflow. (b) RGB color image (in linear scale) with an overlay of the 20 cm continuum emission (0.211 Jy/beam × (0.1, 0.2, 0.3, 0.4, 0.55, 0.7, 0.85, 0.95)). In both the panels, the positions of a 6.7 GHz MME (◇) and an O5–O6 star (⋆) are marked in the figure. The 6.7 GHz MME appears at the center of a bipolar emission. The IRc coinciding with the 6.7 GHz MME (i.e., W42-MME) is clearly seen in the RGB image. The cyan arrows highlight noticeable features, including a bow shock, along a continuous elongated H_2 emission. Apart from the elongated H_2 emission, the black arrows also show H_2 emissions in the south-west and south directions. The long axis of the H_2 nebulosity is aligned with the magnetic field (**B**) at the position angle of ~15° (e.g., Jones et al. 2004). The magnetic field direction is also shown by a thick blue arrow. Note that in the displayed H_2 map, the K-continuum is scaled in order to avoid negative values within the H II region, which has resulted in the under-subtraction of stellar features.

Very Large Telescope (VLT) NIR adaptive-optics images and the stellar counterpart is investigated using mid-infrared images.

2. DATA AND ANALYSIS

2.1. Adaptive-optics Near Infrared Imaging Data

Adaptive-optics imaging data toward 6.7 GHz MME were retrieved from the ESO-Science Archive Facility[3] (ESO proposal ID: 089.C-0455(A); PI: Joao Alves). The images were observed in the K_s-band ($\lambda_c = 2.18 \mu$m, $\Delta\lambda = 0.35 \mu$m) and the L'-band ($\lambda_c = 3.80 \mu$m, $\Delta\lambda = 0.62 \mu$m), using 8.2 m VLT with the NAOS-CONICA (NACO) adaptive-optics system[4] (Lenzen et al. 2003; Rousset et al. 2003). Five K_s frames and six L' frames of 24 and 21 seconds, respectively, were used in this study. These data were reduced using the standard analysis procedure available in IRAF and STAR-LINK packages, as described in detail by Kumar (2013). The astrometry of NACO images was calibrated using the GPS K-band point sources (see Section 2.2 for more details). The plate scales of final processed NACO K_s and L' images were 0″.054/pixel and 0″.027/pixel, respectively, resulting in a resolution of 0″.2 (~760 AU) and 0″.1 (~380 AU), respectively.

2.2. Other Archival Data

We also utilized the multi-wavelength data from different surveys, e.g., the Multi-Array Galactic Plane Imaging Survey (MAGPIS: 20 cm; Helfand et al. 2006), the Galactic Ring Survey (GRS: ^{13}CO($J = 1$–0); Jackson et al. 2006), the APEX Telescope Large Area Survey of the Galaxy (ATLASGAL: 870 μm; Schuller et al. 2009), the *Herschel* Infrared Galactic Plane Survey (Hi-GAL: 70–500 μm; Molinari et al. 2010), the Galactic Legacy Infrared Mid-Plane Survey Extraordinaire (GLIMPSE: 3.6–8.0 μm; Benjamin et al. 2003), the UKIRT Wide-field Infrared Survey for H2 (UWISH2: 2.12 μm; Froebrich et al. 2011), and the UKIRT NIR Galactic Plane Survey (GPS: 1.25–2.2 μm; Lawrence et al. 2007). To obtain a continuum-subtracted H_2 map (hereafter H_2 map), the GPS K-band image was registered and scaled to the UWISH2 narrow-band H_2 (1–0) S(1) 2.12 μm image (resolution ~1″). The H_2 map was smoothed with a Gaussian of sigma ~1 pixel to enhance the faint features. The K-band polarimetric data were obtained from Jones et al. (2004).

3. RESULTS

3.1. Multi-wavelength View Around 6.7 GHz MME

The distribution of molecular H_2 emission is shown in Figure 1(a), where the most prominent extended structure is a continuous elongated emission feature centered on the position of the 6.7 GHz MME. On the northern side, the feature intercepts a bow shock at a projected distance of ~0.52 pc from the 6.7 GHz MME. The explanation of the origin of H_2 emission in W42 is difficult because an O5–O6 star is located at a distance of ~0.22 pc from the MME in the W42 H II region. The presence of H_2 emission can be interpreted by either ultraviolet (UV) fluorescence or shocks. Considering the observed morphology of the H_2 features, we suggest that the elongated H_2 emission is caused by shock, which traces a parsec-scale bipolar H_2 outflow. The presence of the bow shock feature and knots embedded in diffuse emission along the elongated H_2 feature offers further evidence for the shock-

---

[3] http://archive.eso.org/eso_archive_main.html
[4] http://eso.org/sci/facilities/paranal/instruments/naco.html
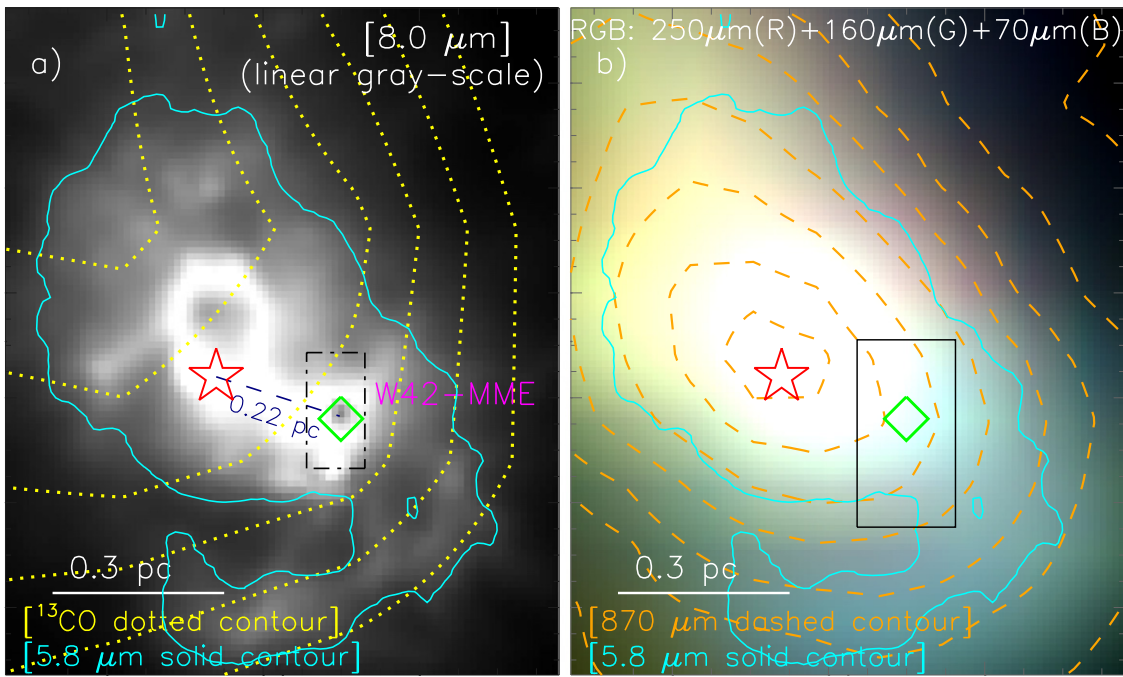
Figure 2. (a) Overlay of the GRS ^{13}CO dotted contours on the 8.0 μm image. A zoomed-in view of the dotted–dashed black box is shown in Figure 4(b). Color composite map using *Herschel* images (in logarithmic scale). The ATLASGAL 870 μm emissions are overlaid by orange contours with 10%, 20%, 30%, 40%, 55%, 70%, 85%, and 95% of the peak value (i.e., 3.3 Jy/beam). A zoomed-in view of the solid black box is shown in Figure 5(a). In both the panels, the other marked symbols are similar to those shown in Figure 1. The boundary of a cavity-like structure is shown by the 5.8 μm cyan contour with a level of 555 MJy sr^{-1} in both of the panels.

excited outflow activity. The overall morphology of the H$_2$ feature resembles the bipolar outflows of Herbig Haro objects. The outflow nature of the observed H$_2$ feature is further supported by the recent detection of [Fe II] emission coinciding with the southwest part (see Figure 12 of Lee et al. 2014). The inner ~0.4 pc part of the H$_2$ outflow has a position angle of ~18°, which coincides with the reflection nebula reported by Jones et al. (2004; see their Figure 5). However, the H$_2$ feature continues much further than the reflection nebula on either side at a position angle of ~40°. Considering the variation in position angles along the outflow, the outflow morphology appears a little twisted in an "S" shape. The GRS ^{13}CO (J = 1–0) line data are unable to provide any outflow signatures toward MME due to a coarse beam (beam size ~45″). Additionally, there are no high-resolution CO observations available in the literature.

In order to identify the IRc of 6.7 GHz MME, we present H$_2$, 3.6, and 5.8 μm images in Figure 1(b). W42-MME is barely detected in the GPS K-band image (not shown here) with an upper limit of ~12.815 mag. It is well detected in GLIMPSE 3.6–5.8 μm images but saturated in the 8.0 μm (see Figures 1(b) and 2(a)). The GLIMPSE-I catalog lists photometric magnitude only in one of the GLIMPSE bands. Therefore, aperture photometry was carried out for W42-MME using the GLIMPSE images (see Dewangan et al. 2015 for more details). The GLIMPSE photometric magnitudes were measured to be 8.295 ± 0.031 (3.6 μm), 6.178 ± 0.012 (4.5 μm), and 4.545 ± 0.103 (5.8 μm) mag. The color excess criteria further reveal this source to be a Class I YSO (see Dewangan et al. 2015 for classification schemes). Figure 1(b) also illustrates the distribution of ionized emission using the MAGPIS 20 cm map (beam size ~6″). It can be seen that the MME-outflow system is immersed within

the W42 H II region. The GRS ^{13}CO(J = 1–0) molecular, ATLASGAL dust continuum at 870 μm (beam size ~19″.2), and *Herschel* sub-millimeter emissions (beam size ~6–18″) are also peaked close to the 6.7 GHz MME position (see Figure 2). These data therefore suggest that W42-MME is located at the densest part of the molecular cloud in W42.

Apart from the elongated bipolar feature, the H$_2$ map also shows H$_2$ emissions in the south-west and south directions, as highlighted by black arrows (see Figure 1(a)). These particular H$_2$ features are nicely coincident with GLIMPSE infrared and 20 cm emissions. In general, GLIMPSE images (3.6–8.0 μm) have been used to trace a photodissociation region around the H II region through the presence of polycyclic aromatic hydrocarbon features at 3.3, 6.2, 7.7, and 8.6 μm. Therefore, it seems that these H$_2$ features (see the black arrows in Figure 1(a)) are formed due to UV fluorescence, tracing the wall of an ionized cavity-like structure (see Figure 1(b)). The ionized cavity-like structure seen in GLIMPSE images is also shown in Figure 2. Interestingly, the bipolar H$_2$ feature in the south direction is further extended beyond the cavity-like structure (Figure 1).

To estimate the stellar mass, we modeled the Spectral Energy Distribution (SED) of W42-MME using an online SED modeling tool (Robitaille et al. 2006, 2007). *Spitzer*-GLIMPSE fluxes at 3.6, 4.5, and 5.8 μm bands were used as data points, whereas GPS K-band magnitude and ATLASGAL 870 μm flux (obtained from Csengeri et al. 2014) were treated as upper limits (e.g., Dewangan et al. 2015). We provided the visual extinction in the range of 0–70 mag and our adopted distance to W42-MME, as input parameters for SED modeling. The fitted SED models of W42-MME are shown in Figure 3(a). The stellar mass distribution for W42-MME is also plotted in
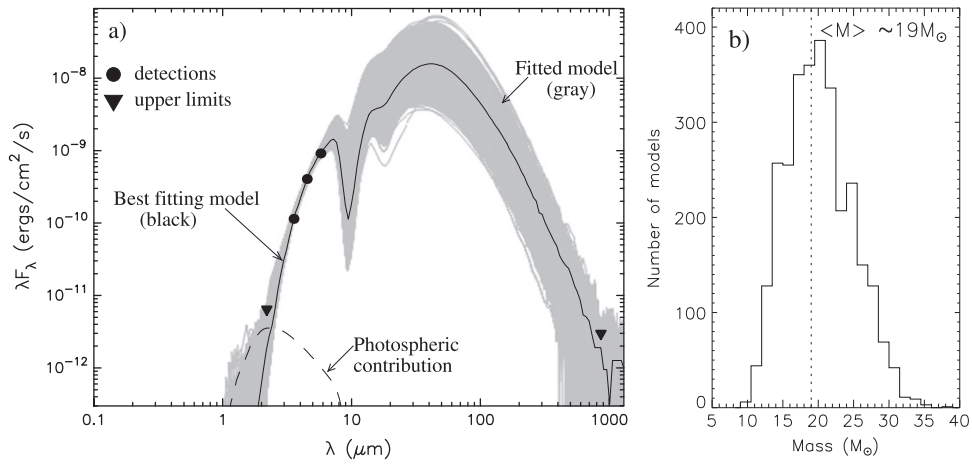
Figure 3. (a) Observed SED (filled symbols) for W42-MME, obtained with the Robitaille et al. ([2006](#)) fitting procedure. Only models that satisfy the condition ($\chi^2 - \chi^2_{\mathrm{best}}$) per data point <3 are selected. The black solid line corresponds to the best fit; the gray solid curves represent all other models providing a good fit to the data. The dashed curve shows photospheric contribution. (b) Distribution of the stellar mass for all plotted models in Figure [3](#)(a). We derive a weighted mean mass of $19 \pm 4\,M_\odot$.
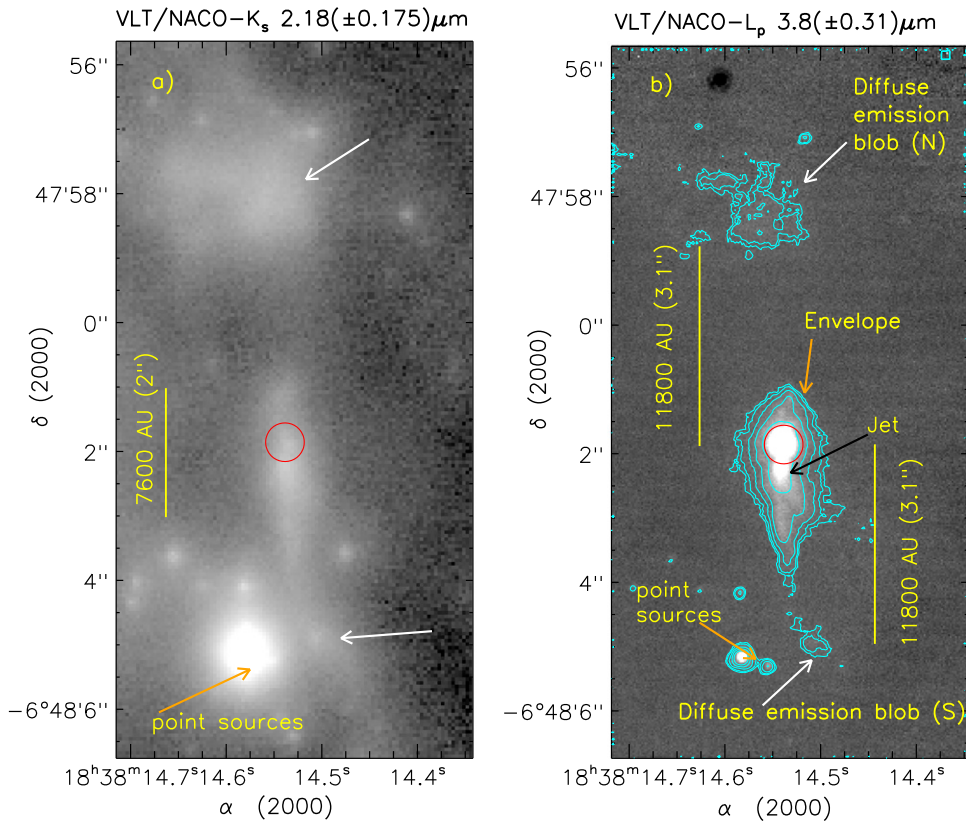
Figure 4. VLT/NACO adaptive-optics images (in logarithmic gray scale) of W42-MME. The selected area of NACO images is shown by a box in Figure [2](#)(a). (a) K_s band. Diffuse emissions are highlighted by white arrows (also see Figure [4](#)(b)). (b) Overlay of L′ contours on the L′ image (the outer most contour corresponds to 4σ, with successive contours increasing logarithmically). In both panels, the position of the driving source ($\alpha_{2000} = 18^h38^m14\overset{s}{.}54$, $\delta_{2000} = -06°48'01\overset{''}{.}86$) is shown by a red circle. Distances of diffuse emissions seen in the L′ image are also highlighted with respect to W42-MME.

Figure [3](#)(b). The weighted mean values of the stellar mass and extinction are $19 \pm 4\,M_\odot$ and 48 ± 15 mag, respectively. The extinction value of W42-MME is consistent with the estimates of Jones et al. ([2004](#)). The weighted mean value of age is found to be 8.1×10^4 yr. Our SED result suggests that W42-MME is an MYSO candidate with a weighted mean luminosity of $4.5 \times 10^4\,L_\odot$. We also fitted the SED assuming a distance of 2.2 kpc and estimated a weighted mean mass of $14 \pm 3\,M_\odot$.

W42-MME is still a massive protostar candidate at a shorter distance of 2.2 kpc. The SED result of W42-MME is also in agreement with the generally accepted argument that the 6.7 GHz methanol masers are solely associated with MSF (e.g., Urquhart et al. [2013](#)).

Taken together, it appears that W42-MME is a driving source of a parsec-scale bipolar outflow and the axis of the outflow is parallel to the magnetic field (see Figure [1](#)).

3.2. Inner Circumstellar Environment of W42-MME

In Figure 4, we show the inner circumstellar environment of W42-MME using the VLT/NACO adaptive-optics images at K_s and L' bands. The K_s image shows diffuse emissions near the position of 6.7 GHz MME, as well as in the north and south directions (see the arrows in Figure 4(a)), which are coincident with the emissions seen in H_2 map. The L' image reveals a point source (i.e., W42-MME) associated with a small-scale feature (within a scale of ~4500 AU). The small-scale feature is noticeably elongated in the vertical direction and the full width half maximum of its point-spread function is almost twice that of other stars seen in the L' image. This comparison allows us to rule out the small-scale feature as a point-like source. W42-MME is also surrounded by an envelope-like emission, which is extended on a physical scale of ~10640 AU, oriented along the north–south direction.

Zhang & Tan (2011) performed the radiative transfer calculations to understand the observed NIR and mid-infrared emissions around embedded MYSOs. They suggest that the outflow cavity is the most significant feature in images up to 70 μm. They also find that the NIR emission is mainly due to scattered light from the outflow cavity wall. Using the prediction model, we consider the envelope-like structure as an outflow cavity traced by the scattered light. The cavity has a very narrow opening tip at both ends and is more extended (~4900 AU in east–west) near the position of W42-MME (see Figure 4(b)).

In both NACO images, the diffuse emissions are found parallel to the cavity in the north and south directions, which are separated by a similar distance of ~3″.1 (~11,800 AU) with respect to W42-MME. This provides evidence for the presence of a symmetric configuration along the flow axis. The physical association of the small-scale feature, the cavity, and the outflow is shown in Figure 5(a). In the north direction, the H_2 knot is coincident with the tip of the cavity along the flow axis. All of these observed features suggest that they can originate from the interaction of a jet with the molecular gas in its surroundings. Therefore, the small-scale feature within the cavity is evidence of a jet associated with MYSO W42-MME (see Figure 5(b) for a zoomed-in view).

Considering together the observed emissions, the NACO L' image traces the inner part of the outflow, which is highly collimated to a small-angle jet. A zoomed-in view of the cavity and the jet using a two color composite NACO image (red:L' and green:K_s) is shown in Figure 5(b). The IRc and the cavity have red colors suggesting the absence of K_s emission from these parts. It also appears that the cavity resembles an onion-like structure. The jet is bright in the L' image, which encompasses the Brα (4.05 μm) line emission as the main contributor. Therefore, we suggest that it is an ionized jet associated with a driving source W42-MME. The K_s diffuse emission is also coincident with a jet-like feature located within the cavity, which could be due to the Brγ (2.166 μm) line emission. In order to further investigate the ionized nature of the jet, we estimated the emission measure (EM) of the jet feature using its photometric fluxes obtained in both the NACO images. The photometric calculations of the jet-feature were performed with the removal of its surrounding diffuse emission. In the calculation of EM, we assume that the whole jet emission is dominated by the hydrogen lines. Therefore, the K_s and L' fluxes of the jet feature provide a measure of the Brγ and Brα line emissions, respectively.

Following the recombination theory and the observed flux ratio of Brα to Brγ, we computed the extinction of Brα and Brγ emissions (see the Appendix in Ho et al. 1990, and references therein). The intrinsic flux ratio of Brα to Brγ was adopted for Case B with $T_e = 10^4$ K and $n_e = 10^4$ cm^{-3}. Following the Indebetouw et al. (2005) extinction law, the visual extinction (A_V) of jet emission is also estimated to be about 37 mag using the extinction at Brγ emission, which is in agreement with our SED result. Furthermore, the extinction corrected Brγ flux is used to measure the EM of ~2.7×10^9 cm^{-6} pc (see Tokunaga & Thompson 1979 for the equation), which can be taken as an indicative value. Our estimate of EM is consistent with the values obtained for candidate radio jets toward MYSOs (e.g., Guzmán et al. 2012). It is also to be noted that the magnetic field is parallel to the jet-outflow axis (see Figure 5(a)). In the south direction, the blob emissions and the tip of the cavity are not perfectly aligned with the H_2 outflow axis. Furthermore, the H_2 outflow has a little bend with respect to the jet axis. It further suggests the variation in position angles from small scale to large scale along the outflow axis.

3.3. Summary and Discussion

We studied the inner circumstellar environment of a deeply embedded IRc of 6.7 GHz MME in W42 (i.e., W42-MME), as the driving source of a parsec-scale bipolar H_2 outflow. The parsec-scale H_2 outflow morphology appears a little twisted in an "S" shape, with the position angle changing smoothly from ~18° near the IRc to ~40° at the ends. W42-MME is characterized as an MYSO with a mass of $19 \pm 4\,M_\odot$. This is the first time we identified W42-MME and characterized its stellar mass. The aim of this work was to understand the jet/outflow formation process in MSF. We discovered a collimated jet in the inner 4500 AU in W42-MME using the L' band to which the Brα line emission contributes prominently, suggesting that the jet is ionized in nature. The presence of the jet was further confirmed by the detection of bow shock feature and knots in diffuse emission in the H_2 map along the flow axis (i.e., jet-related features). The jet is found inside a cavity (extent ~10640 AU) oriented along the north–south direction, which is tapered at both ends. Such a morphology appears to be responsible for collimating the jet/outflow. The diffuse nebular blobs seen in the north and south directions are located at similar distances (~11800 AU) from W42-MME, which can be considered as a symmetric configuration along the flow axis. The previously published magnetic field direction is parallel to the jet-outflow flow axis.

All of these observed characteristics at a few thousands AU and a parsec-scale share some common features of the jet-driven bow shock model, the precessing jet model, and the magnetically driven model (e.g., Arce et al. 2007; Pudritz et al. 2007, and references therein). In summary, a detailed modeling is needed to pinpoint the exact physical mechanism for the W42-MME jet-outflow system.

The high angular resolution of NACO images around an MYSO W42-MME have enabled the detection of the inner jet-outflow configuration. Such a system is hardly known and is crucial for understanding the jet-outflow formation process. We find that the morphology of outflow cavity in W42-MME is unique and rare, which is not seen at the inner environment of some well-studied low and massive stars (e.g., Fuller et al. 2001; Valusamy et al. 2007; Carrasco-González et al. 2010).
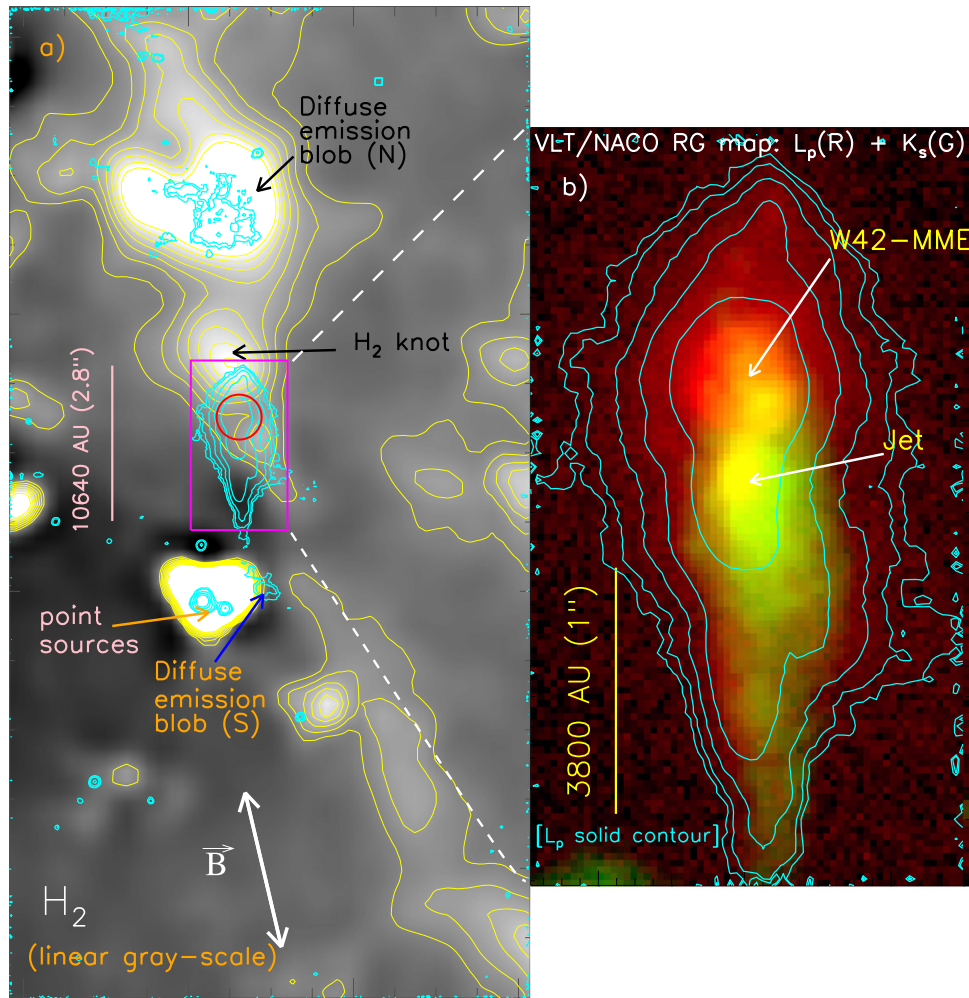
Figure 5. (a) Overlay of L′ contours (in cyan color) on the continuum-subtracted H₂ image at 2.12 μm. The selected area of the H₂ image is shown by a box in Figure 2(b). The L′ contours are similar to those shown in Figure 4(b). The H₂ contours (in yellow) are superimposed in order to highlight faint H₂ features. The magnetic field (**B**) direction is also shown as Figure 1(a). (b) Zoomed-in view of a two color composite NACO image (in logarithmic gray scale), which clearly illustrates the morphology of the cavity and the jet.

Therefore, the inferred spatial morphology of W42-MME can be used to constrain the jet launching and jet collimation models in MSF.

REFERENCES

Anderson, L. D., Bania, T. M., Jackson, J. M., et al. 2009, ApJS, 181, 255
Arce, H. G., Shepherd, D., Gueth, F., et al. 2007, in Protostars and Planets V, ed. B. Reipurth, D. Jewitt, & K. Keil (Tucson, AZ: Univ. Arizona Press), 245
Benjamin, R. A., Churchwell, E., Babler, B. L., et al. 2003, PASP, 115, 953
Beuther, H., Schilke, P., Menten, K. M., et al. 2002, ApJ, 566, 945
Beuther, H., Walsh, A. J., & Longmore, S. N. 2009, ApJS, 184, 366
Blum, R. D., Conti, P. S., & Damineli, A. 2000, AJ, 119, 1860
Carrasco-González, C., Rodríguez, L. F., Anglada, G., et al. 2010, Sci, 330, 1209
Csengeri, T., Urquhart, J. S., Schuller, F., et al. 2014, A&A, 565, 75
Dewangan, L. K., Ojha, D. K., Grave, J. M. C., & Mallick, K. K. 2015, MNRAS, 446, 2640
Froebrich, D., Davis, C. J., Ioannidis, G., et al. 2011, MNRAS, 413, 480
Fuller, G. A., Zijlstra, A. A., & Williams, S. J. 2001, ApJL, 555, L125
Guzmán, A. E., Garay, G., & Brooks, K. J. 2010, ApJ, 725, 734
Guzmán, A. E., Garay, G., Brooks, K. J., & Voronkov, M. A. 2012, ApJ, 753, 51
Helfand, D. J., Becker, R. H., White, R. L., Fallon, A., & Tuttle, S. 2006, AJ, 131, 2525
Ho, P. T. P., Beck, S. C., & Turner, J. L. 1990, ApJ, 349, 57
Indebetouw, R., Mathis, J. S., Babler, B. L., et al. 2005, ApJ, 619, 931
Jackson, J. M., Rathborne, J. M., Shah, R. Y., et al. 2006, ApJS, 163, 145
Jones, T. J., Woodward, C. E., & Kelley, M. S. 2004, ApJ, 128, 2448
Kumar, M. S. N. 2013, A&A, 558, 119
Lada, C. J. 1985, ARA&A, 23, 267
Lawrence, A., Warren, S. J., Almaini, O., et al. 2007, MNRAS, 379, 1599
Lee, J. J., Koo, B. C., Lee, Y. H., et al. 2014, MNRAS, 443, 2650
Lenzen, R., Hartung, M., Brandner, W., et al. 2003, Proc. SPIE, 4841, 944
Lester, D. F., Dinerstein, H. L., Werner, M. W., et al. 1985, AJ, 296, 565
Molinari, S., Swinyard, B., Bally, J., et al. 2010, A&A, 518, L100
Pudritz, R. E., Ouyed, R., Fendt, C., & Brandenburg, A. 2007, Protostars and Planets V, ed. B. Reipurth, D. Jewitt, & K. Keil (Tucson, AZ: Univ. Arizona Press), 277
Robitaille, T. P., Whitney, B. A., Indebetouw, R., Wood, K., & Denzmore, P. 2006, ApJS, 167, 256
Robitaille, T. P., Whitney, B. A., Indebetouw, R., & Wood, K. 2007, ApJS, 169, 328
Rousset, G., Lacombe, F., Puget, P., et al. 2003, Proc. SPIE, 4839, 140

Schuller, F., Menten, K. M., Contreras, Y., et al. 2009, A&A, 504, 415

Szymczak, M., Wolak, P., Bartkiewicz, A., & Borkowski, K. M. 2012, AN, 333, 634

Tokunaga, A. T., & Thompson, R. I. 1979, ApJ, 229, 583

Urquhart, J. S., Moore, T. J. T., Schuller, F., et al. 2013, MNRAS, 431, 1752

Valusamy, T., Langer, W. D., & Marsh, K. A. 2007, ApJL, 668, L159

Walsh, A. J., Burton, M. G., Hyland, A. R., & Robinson, G. 1998, MNRAS, 301, 640

Wu, Y., Wei, Y., Zhao, M., et al. 2004, A&A, 426, 503

Zhang, Q., Hunter, T. R., Brand, J., et al. 2005, ApJ, 625, 864

Zhang, Y., & Tan, J. C. 2011, ApJ, 733, 55